Equivalent-Circuit Model for Quartz Resonators Effects of Finite Element Analysis, Acceleration, and Mass Loading

Rabie Meftah, Yann Meyer

Equivalent-Circuit Model for Quartz Resonators Effects of Finite Element Analysis, Acceleration, and Mass Loading

R. MEFTAH and Y. MEYER

Institut Superieur de Mecanique de Paris (SUPMECA Paris), LISMMA/Structures, Saint Ouen Cedex, France

In radar equipments and communication systems, quartz resonators are key components. So as to enhance the resonator performances, the development of accurate modelings taking into account the environment interaction (temperature, acceleration, magnetism, ...) is one of the major economic and strategic stakes. The main idea is to produce a realistic modeling. In literature, a lot of modelings are based on finite element analysis. But, for industrial applications, it is essential to link these accurate modelings to electric simulation softwares, such as Spice. Moreover, it is necessary to develop a simple computation method in order to answer the industrial time constraints. The idea is to use a Butterworth-Van Dyke (BVD) model based on an electrical equivalent circuit with, as input data, the studied natural frequency and the antiresonance frequency of an accurate finite element modeling. For the numerical example, a SC-cut (Stress-Compensated cut) quartz resonator is studied in this article for its fundamental thickness-shear resonance, the third and the fifth overtone. The influence of the model mesh quality, the electrode mass-loading, and the acceleration sensitivity on the motional parameters are analyzed. First, the choice of the finite element number along the thickness axis is crucial for the computation accuracy of the motional parameters. Then, the more the electrode material has a high density, the more the mass loading has a strong influence of the motional parameter values. Finally, the motional parameters are not really influenced by the acceleration field.

Keywords: resonator, bulk acoustic wave, quartz, thickness-shear mode, acceleration sensitivity, mass loading, frequency stability

1. Introduction

Quartz resonators are key components of many guidance systems, radar equipments, and communication devices. A resonator is a resonant device operating at a specific frequency. Generally, these resonators are based on thickness-shear modes. The thickness shear modes appear in high frequencies. These modes correspond to small displacements along the crystalline plans, which slip the ones compared to the others, as illustrated in Figure 1. This figure shows also the various overtones of these thickness-shear modes. With these frequencies, a precise time can be obtained. Then, a precise synchronization or an accurate identification can be performed. But, a resonator, and so its resonant frequency, is very sensitive to a wide range of environment parameters as temperature, acceleration, magnetism, vibrations, shocks, etc. [1–3]. This drawback affects stability and accuracy of equipments by producing large phase noise and frequency deviations.

For precise time applications, the key properties are a good temperature stability, a high quality factor, and a low acceleration sensitivity. Compared to the other piezoelectric materials, the quartz crystal provides an interesting combination of properties. The quartz material properties are highly repeatable, manufacturable, and extremely stable with respect to the temperature shifts and aging. The frequency temperature coefficient can be limited by a precise crystal cut (AT-cut, BT-cut, SC-cut, etc.) [4–6]. Intrinsically, the quartz structures have limited the changes of material properties over a given period of time [7]. For example, the common aging rate for commercial quartz resonators is approximatively 5 ppm (parts per million) per year. Moreover, the internal losses of quartz material are very low [8]. Consequently, an intrinsic quality factor of about 10^7 at 1 MHz can be easily obtained. To achieve a resonator with low acceleration sensitivity, the first activity is based on the modification of the resonator support by working on the assembly process and geometrical optimization [9, 10]. The second way to improve a vibratory behavior is to use a control process by modifying the DC bias with respect to acceleration [11] or by introducing, onto crystal device, actuating electrodes to actively control the structure [12]. All these improvements are found on a mathematical modeling of quartz structures and, also, of ambient phenomenons.

In the literature, one of the major issues is the improvement of the resonator numerical modeling by taking into account environment. Indeed, the improvement of the resonator frequential stability is currently a major economic and strategic stake. The main idea is to produce a realistic modeling. For example, Yong and et al. [13] study the impact of a finite element analysis on the resonator properties. Taking into account the resonator losses is analyzed by Lee and et al. [14]. The thermal

Address correspondence to Y. Meyer, Institut Superieur de Mecanique de Paris (SUPMECA Paris), LISMMA/Structures, 3, rue Fernand Hainaut, Saint Ouen Cedex, 93407, France. E-mail: yann.meyer@gmail.com

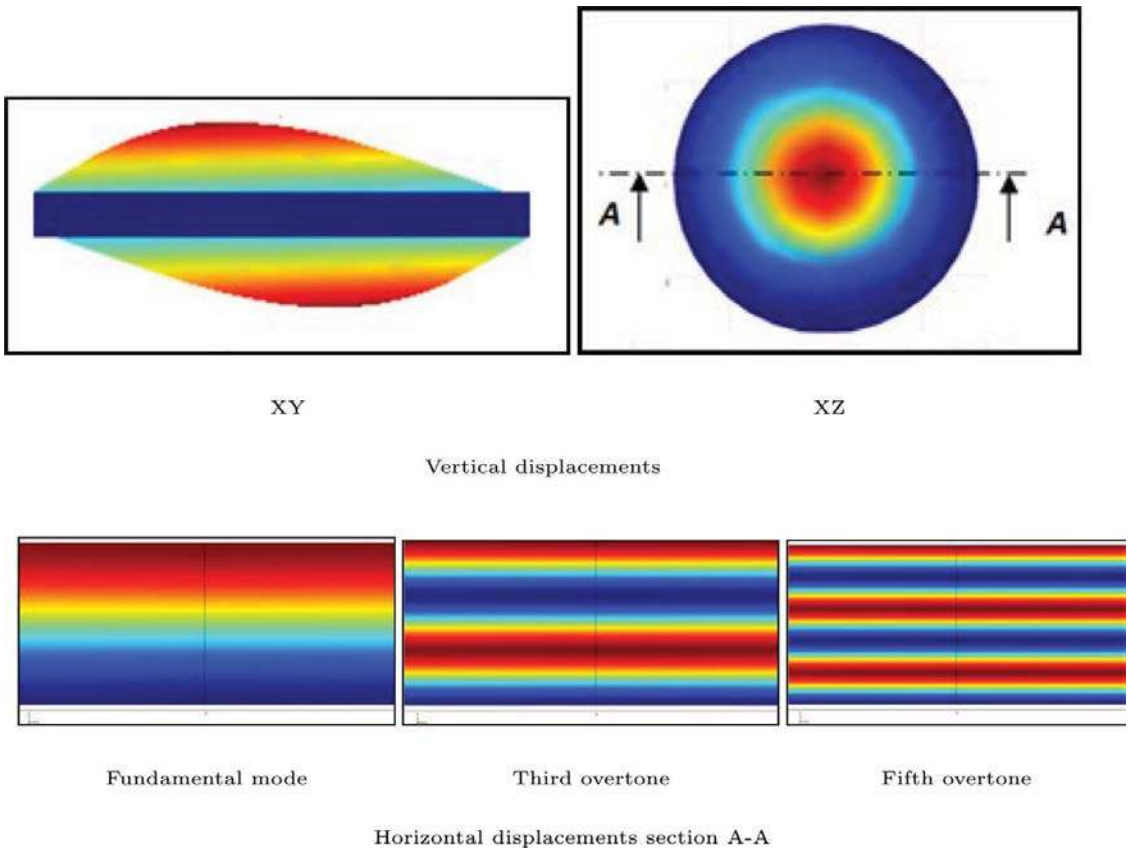

Fig. 1. Thickness shear modes (color figure available online).

effects on the resonator frequency value [15] or the impact of the geometrical nonlinearities on the quartz device [16] are also studied. All these accurate studies are based on finite element analysis. But, for an industrial application, it is necessary to link these accurate modelings to electric simulation softwares, such as Spice, for example. So, it's crucial to develop a simple computation method in order to answer at the industrial time constraints. The idea is to use a Butterworth-Van Dyke (BVD) model based on an electrical equivalent circuit with, as input data, the natural frequencies of an accurate finite element model. These electric parameters are called motional parameters of the quartz resonator. This process is well-known. But, the environment and computation influence on the behavior of the motional parameters is rarely studied in the literature [17].

The objective of this article is to study the influence of the model mesh quality, the electrode mass-loading, and the acceleration sensitivity on the motional parameters of a quartz resonator. A SC-cut quartz resonator is studied in this article for its fundamental thickness-shear resonance, the third and the fifth overtone. For the numerical process, the authors make the choice of a 3D implementation. It is clearly not the optimal way of modeling in terms of computation time and accuracy. However, it seems to be more understandable and currently sufficient for a large industrial use.

The article is organized as follows. Section 2 describes a thickness-shear mode resonator, made of quartz, and gives relevant information about the studied structure. In Section 3, the piezoelectric linear formulation, applied to quartz material, and the finite element discretization of the resonator is provided. The BVD model, based on the computation of the motional parameters, is detailed. In the following section, the finite element analysis optimization is performed for the studied resonator. The model mesh influence on the motional parameters is studied for the fundamental frequency, the third overtone, and the fifth overtone. The mass-loading effects on the motional parameters are investigated and compared for three modelings: two modeling taking into account the electrodes mass and one modeling without electrodes, in Section 5. Several electrode materials are also studied. Section 6 presents the acceleration sensitivity influence on the motional parameters along an out-plan axis and radial axis. A confrontation between the experimental data and the numerical data is exposed in Section 7. Finally, concluding remarks are discussed.

2. Thickness-Shear Mode Resonator

The studied thickness-shear mode resonator is a 120 MHz resonator. A close-up of a representative Computer Aided Design resonator is given in Figure 2. This resonator is a bi-plane quartz plate with a "stress-compensated" cut crystal (SC-cut crystal). The structure has a circular shape. The resonator dimensions are given in Figure 3. A specific geometrical

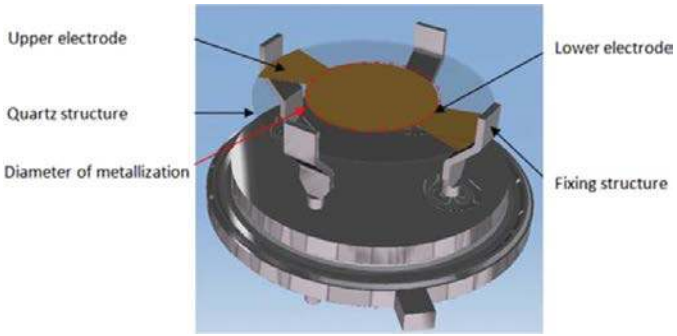

Fig. 2. Representative Computer Aided Design resonator (color figure available online).

coordinate system is linked to the resonator. This coordinate system is presented in Figure 4.

3. Numerical Modeling

3.1. *Governing Equations*

In a structural domain Ω_0, the mechanical displacement **u** and the electric potential V satisfy the stress equations of motion (Navier's equation) and the Gauss' law of electrostatics.

$$\sigma_{ij,i} + \mathbf{f}_j = \rho \ddot{\mathbf{u}}_j, \tag{1}$$
$$\mathbf{D}_{i,i} = \rho_e = 0, \tag{2}$$

where σ represents the mechanical stress tensor (N.m^{-2}), **D** the electric displacement (C.m^{-2}), ρ the mass density (kg.m^{-3}), ρ_e the volume charge density (C.m^{-3}), and **f** the external volume force density (N.m^{-3}).

The associated mechanical boundary conditions are:

$$\begin{cases} \mathbf{u} = \mathbf{u}_0 & \forall x \in \partial\Omega_0^u \\ \mathbf{n}_i \sigma_{ij} = \bar{\mathbf{t}}_j & \forall x \in \partial\Omega_0^T \end{cases}, \tag{3}$$

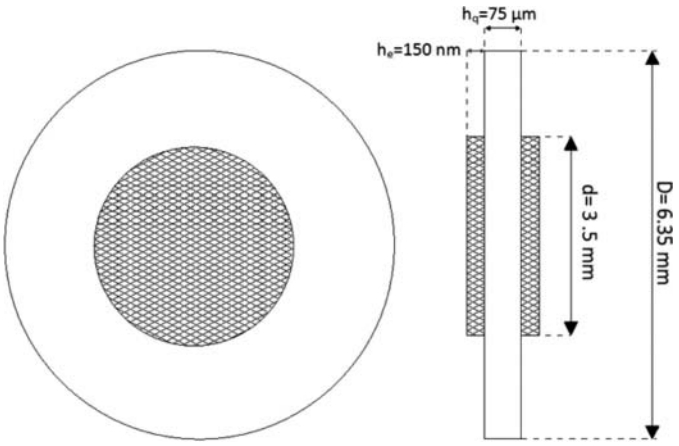

Fig. 3. Thickness-shear mode resonator.

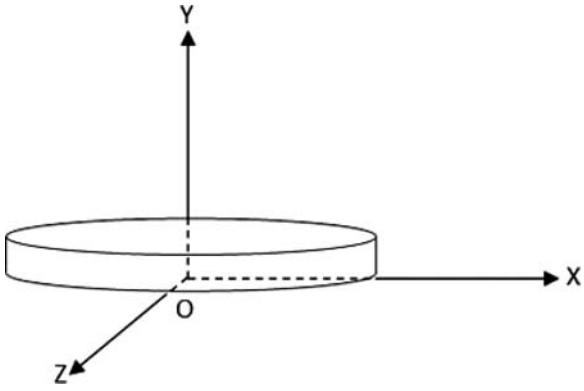

Fig. 4. Geometrical coordinate system for the quartz resonator.

where $\partial\Omega_0^u$ and $\partial\Omega_0^T$ represent respectively Dirichlet mechanical conditions and Neumann mechanical conditions and **n** an outward normal vector at $\partial\Omega_0^T$.

The associated electric boundary conditions are:

$$\begin{cases} V = 0 & \forall x \in \partial\Omega_0^V \\ V = V_a & \forall x \in \partial\Omega_a^V \\ [\mathbf{n}_i \mathbf{D}_i] = 0 & \forall x \in \partial\Omega_0^q \end{cases}, \tag{4}$$

where $\partial\Omega_0^V$, $\partial\Omega_a^V$, and $\partial\Omega_0^q$ represent respectively the Dirichlet electrical conditions, the Dirichlet electrical conditions at input/output electrical surfaces, and the Neumann electrical conditions and **n** an outward normal vector at $\partial\Omega_0^q$.

3.2. *Quartz Crystal Constitutive Equations*

In order to determine the solution of the piezoelectric vibration problem, the arrays of material coefficient for the particular symmetry of quartz crystal have to be known. Because of their symmetry, the mechanical stress and strain tensors can be brought together in stress **T** and strain **S** vectors containing six independent values by using the compressed matrix notation (IEEE standard).

The piezoelectric behavior law can be described by tensor relations. These equations express the main constitutive formulations between stress and strain tensors. If the magnetic and thermal effects are considered negligible, the multiphysics relationships are written in a compressed matrix notation as follows:

$$\mathbf{T}_p = c_{pq}^E \mathbf{S}_q - e_{kp} \mathbf{E}_k, \tag{5}$$
$$\mathbf{D}_i = e_{iq} \mathbf{S}_q + \varepsilon_{ik}^S \mathbf{E}_k, \tag{6}$$

where $\mathbf{E} = -\nabla V$.

c^E, ε^S, e, and **E** are respectively the elasticity matrix at constant electric field (N.m^{-2}), the dielectric permittivity matrix at constant strain (F.m^{-1}), the quartz electromechanical coupling matrix (C.m^{-2}), and the electric field vector (V.m^{-1}). The coefficients of matrices (7), (8), and (9) are extracted from [18].

The mass density of quartz crystal is 2648 kg.m^{-3}.

$$e_{kp} = \begin{bmatrix} e_{11} & -e_{11} & 0 & e_{14} & 0 & 0 \\ 0 & 0 & 0 & 0 & -e_{14} & -e_{11} \\ 0 & 0 & 0 & 0 & 0 & 0 \end{bmatrix}, \tag{7}$$

where $e_{11} = 0.171$ and $e_{14} = -0.046$;

$$c^E_{pq}[10^{10}] = \begin{bmatrix} c_{11} & c_{12} & c_{13} & c_{14} & 0 & 0 \\ c_{12} & c_{11} & c_{13} & -c_{14} & 0 & 0 \\ c_{13} & c_{13} & c_{33} & 0 & 0 & 0 \\ c_{14} & -c_{14} & 0 & c_{44} & 0 & 0 \\ 0 & 0 & 0 & 0 & c_{44} & c_{14} \\ 0 & 0 & 0 & 0 & c_{14} & \dfrac{c_{11} - c_{12}}{2} \end{bmatrix}, \tag{8}$$

where $c_{11} = 8.67, c_{12} = 0.7, c_{13} = 1.19, c_{14} = -1.79, c_{33} = 10.72,$ and $c_{44} = 5.79$; and

$$\varepsilon^S_{ik}[10^{-11}] = \begin{bmatrix} \varepsilon_{11} & 0 & 0 \\ 0 & \varepsilon_{11} & 0 \\ 0 & 0 & \varepsilon_{33} \end{bmatrix}, \tag{9}$$

where $\varepsilon_{11} = 3.91$ and $\varepsilon_{33} = 4.1$.

The rotations, defining crystal cut, have to be applied to the electromechanical coupling matrix, the permittivity matrix, and the elasticity matrix, as defined in relationships (10). An easy way to perform these rotations is the use of a Bond matrix [19]. The Bond matrix, M, is a matrix composed of the classical rotation matrix, a, but each quadrant of the Bond matrix is a combination of the classical rotations matrix.

$$\begin{aligned} e^* &= ae\, M^T, \\ c^{E*} &= Mc^E M^T, \\ \varepsilon^{S*} &= a\varepsilon^S a^T. \end{aligned} \tag{10}$$

3.3. *Finite Element Discretization*

By combining the relationships from (1) to (6), a set of equations, related to the modeling of the studied structure, is obtained. According to [20], the weak formulation associated with this model is expressed. Then, the finite element method is applied for discretization. Finally, the finite element formulation is given in (11) under a matrix form:

$$\begin{pmatrix} K_{\mathbf{uu}} & K_{\mathbf{uV}_i} & K_{\mathbf{uV}_p} \\ K^t_{\mathbf{uV}_i} & -K_{\mathbf{V}_i\mathbf{V}_i} & -K_{\mathbf{V}_i\mathbf{V}_p} \\ K^t_{\mathbf{uV}_p} & -K^t_{\mathbf{V}_i\mathbf{V}_p} & -K_{\mathbf{V}_p\mathbf{V}_p} \end{pmatrix} \begin{pmatrix} \mathbf{u}_n \\ \mathbf{V}_i \\ \mathbf{V}_p \end{pmatrix} + \begin{pmatrix} M_{\mathbf{uu}} & 0 & 0 \\ 0 & 0 & 0 \\ 0 & 0 & 0 \end{pmatrix} \begin{pmatrix} \ddot{\mathbf{u}}_n \\ \ddot{\mathbf{V}}_i \\ \ddot{\mathbf{V}}_p \end{pmatrix} = \begin{pmatrix} \mathbf{F} \\ \mathbf{0} \\ \mathbf{Q} \end{pmatrix}, \tag{11}$$

where $\mathbf{V}_p$, $\mathbf{V}_i$, $\mathbf{u}_n$, $M_{\mathbf{uu}}$, $K_{\mathbf{uu}}$, $K_{\mathbf{uV}_*}$, $K_{\mathbf{V}_i\mathbf{V}_*}$ and $K_{\mathbf{V}_*\mathbf{V}_*}$ represent respectively the nodal electrical potential vector applied to $\partial\Omega^V_a$ (V), the unknown nodal electrical potential vector interior to each piezoelectric domain (V), the nodal displacement vector (m), the mass matrix (kg), the elastic stiffness matrix (N.m^{-2}), the piezoelectric stiffness matrices (C.m^{-2}), and the dielectric stiffness matrix (F.m^{-1}). $\mathbf{F}$ and $\mathbf{Q}$ are respectively the mechanical force vector applied to the nodes of the structure (N) and the electric charge vector measured in $\partial\Omega^V_a$ (C).

A Guyan-type static condensation is performed so as to keep only the electrical potential vector, $\mathbf{V}_p$. From the second line of Eq. (11), the unknown nodal electric field vector is extracted.

$$\mathbf{V}_i = K^{-1}_{\mathbf{V}_i\mathbf{V}_i}\left(K^t_{\mathbf{uV}_i}\mathbf{u}_n - K_{\mathbf{V}_i\mathbf{V}_p}\mathbf{V}_p\right). \tag{12}$$

By combining Eqs. (12) and (11), relationship (13) is obtained:

$$\begin{pmatrix} H_{\mathbf{uu}} & H_{\mathbf{uV}_p} \\ H^t_{\mathbf{uV}_p} & -H_{\mathbf{V}_p\mathbf{V}_p} \end{pmatrix} \begin{pmatrix} \mathbf{u}_n \\ \mathbf{V}_p \end{pmatrix} + \begin{pmatrix} M_{\mathbf{uu}} & 0 \\ 0 & 0 \end{pmatrix} \begin{pmatrix} \ddot{\mathbf{u}}_n \\ \ddot{\mathbf{V}}_p \end{pmatrix} = \begin{pmatrix} \mathbf{F} \\ \mathbf{Q} \end{pmatrix}, \tag{13}$$

with

$$\begin{cases} H_{\mathbf{uu}} = K_{\mathbf{uu}} + K_{\mathbf{uV}_i}K^{-1}_{\mathbf{V}_i\mathbf{V}_i}K^t_{\mathbf{uV}_i} \\ H_{\mathbf{uV}_p} = K_{\mathbf{uV}_p} - K_{\mathbf{uV}_p}K^{-1}_{\mathbf{V}_i\mathbf{V}_i}K^t_{\mathbf{V}_i\mathbf{V}_p} \\ H_{\mathbf{V}_p\mathbf{V}_p} = K^t_{\mathbf{V}_p\mathbf{V}_p} + K^t_{\mathbf{V}_i\mathbf{V}_p}K^{-1}_{\mathbf{V}_i\mathbf{V}_i}K_{\mathbf{V}_i\mathbf{V}_p} \end{cases}.$$

It is necessary to apply the equipotentiality condition to the electrodes. Indeed, the electric potential has the same value anywhere on an electrode. Equation (14) traduces this condition:

$$\mathbf{V}_p = I_v\mathbf{V}_a, \tag{14}$$

where I_v is a locating matrix composed of 1 and 0.

Relationship (14) is applied to system (15):

$$\begin{pmatrix} H_{\mathbf{uu}} & H_{\mathbf{uV}_a} \\ H^t_{\mathbf{uV}_a} & -H_{\mathbf{V}_a\mathbf{V}_a} \end{pmatrix} \begin{pmatrix} \mathbf{u}_n \\ \mathbf{V}_a \end{pmatrix} + \begin{pmatrix} M_{\mathbf{uu}} & 0 \\ 0 & 0 \end{pmatrix} \begin{pmatrix} \ddot{\mathbf{u}}_n \\ \ddot{\mathbf{V}}_a \end{pmatrix} = \begin{pmatrix} \mathbf{F} \\ \mathbf{q}_a \end{pmatrix}, \tag{15}$$

where

$$\begin{cases} H_{\mathbf{uV}_a} = H_{\mathbf{uV}_p}I_v \\ H_{\mathbf{V}_a\mathbf{V}_a} = I^t_v H_{\mathbf{V}_p\mathbf{V}_p}I_v \\ \mathbf{q}_a = I^t_v\mathbf{Q} \end{cases}.$$

$H_{\mathbf{V}_a\mathbf{V}_a}$ is a diagonal matrix composed of the equivalent electric capacities of the piezoelectric patches and $\mathbf{q}_a$ the

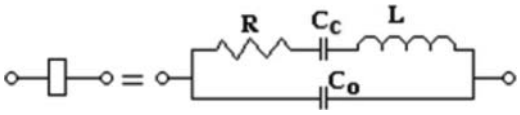

Fig. 5. Equivalent circuit of the quartz resonator.

electric charge vector measured at the surface of the piezoelectric patches.

If $\mathbf{F} = \mathbf{0}$ is assumed, the set of Eq. (15) can be written as follows:

$$M_{\mathbf{uu}}\ddot{\mathbf{u}}_n + (H_{\mathbf{uu}} + \Delta H_{\mathbf{uu}})\mathbf{u}_n = H_{\mathbf{uV}_a} H^{-1}_{\mathbf{V}_a\mathbf{V}_a}\mathbf{q}_a, \tag{16}$$

$$H^{-1}_{\mathbf{V}_a\mathbf{V}_a} H^{t}_{\mathbf{uV}_a}\mathbf{u}_n - H^{-1}_{\mathbf{V}_a\mathbf{V}_a}\mathbf{q}_a = \mathbf{V}_a, \tag{17}$$

where

$$\Delta H_{\mathbf{uu}} = H_{\mathbf{uV}_a} H^{-1}_{\mathbf{V}_a\mathbf{V}_a} H^{t}_{\mathbf{uV}_a}.$$

3.4. *Equivalent Circuit Model*

The equivalent circuit, presented in Figures 5 and 6, depicts the electric activity of a quartz crystal unit operating at its natural resonant frequency. The C_0 represents the static capacitance of the crystal. R, Cs, and L compose the dynamical circuit of the crystal, and are called motional parameters. An electromechanical equivalency can be performed. The motional inductance (L) represents the vibrating mass of the crystal unit. The motional capacitance (C_c) represents the elasticity of quartz, and the resistance (R), represents the bulk losses occurring within quartz. Let's note that the motional parameters are input data for the electric simulation software. Thus, the knowledge of these parameters is essential.

The static capacitance can be given by the geometrical parameters of the quartz structure. It is the ratio between the electric potential, V_0, and the electric charge, q_0. In electrostatics, for a structure mechanically free, Eq. (6) becomes:

$$\mathbf{D}_i = \varepsilon^T_{ik}\mathbf{E}_k. \tag{18}$$

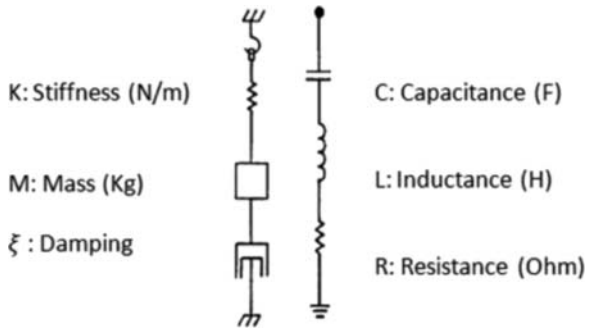

Fig. 6. Equivalent electromechanical parameters.

The electric charge is given by the relationship (19):

$$q = \iint_s \mathbf{D}.\mathbf{n}\, ds, \tag{19}$$

where $\mathbf{n}$ is the normal vector and s the quartz structure surface (m^2).

$$q = -\iint_s \begin{bmatrix} \varepsilon^T_{11} & 0 & 0 \\ 0 & \varepsilon^T_{22} & \varepsilon^T_{23} \\ 0 & \varepsilon^T_{32} & \varepsilon^T_{33} \end{bmatrix} \begin{bmatrix} 0 \\ E2 \\ 0 \end{bmatrix} . \begin{bmatrix} 0 \\ 1 \\ 0 \end{bmatrix} ds. \tag{20}$$

By assuming that the electric field is linear along the thickness axis of the structure, Eq. (21) can be written:

$$q = \frac{s}{h}\varepsilon^T_{22} V. \tag{21}$$

Finally, the static capacitance can be given by relationship (22):

$$C_0 = \frac{s}{h}\varepsilon^T_{22} = \frac{s}{h}\varepsilon^T_{r_{22}}\varepsilon_0, \tag{22}$$

where ε_{22}, ε^T_{r22}, and ε_0 are respectively the absolute permittivity, the quartz permittivity in vacuum, and the vacuum permittivity ($\varepsilon_0 = 8.86\,\mathrm{pF/m}$). As quartz is a very low coupling material, $\varepsilon^T_{r22} \approx \varepsilon^S_{r22}$. So, the static capacitance of the studied quartz structure is $C_0 = 5.1pF$.

To compute the motional parameters C_c and L, two eigenvalue simulations are achieved. The mechanical boundary condition is the clamping of the quartz device side surface.

For the first computation, the electrodes are open-circuited, as shown in Figure 7a. The electric voltage between the electrodes is given by Eq. (23):

$$V_a = u_R + u_L + u_c = 0, \tag{23}$$

where u_R, u_L, and u_c are respectively the electric voltage (V) in the resistance, the inductance, and the capacitance. Then, these different voltages are given by Eq. (24):

$$u_R = Ri = RC_c\frac{du_c}{dt},$$
$$u_L = L\frac{di}{dt} = LC_c\frac{d^2u_c}{dt^2}. \tag{24}$$

Relationship (25) is the differential equation of u_c:

$$LC_c\frac{d^2u_c}{dt^2} + RC_c\frac{du_c}{dt} + u_c = 0. \tag{25}$$

For a conservative system ($R = 0$), the natural frequency is given by Eq. (26). The motional resistance can be calculated with the consideration of viscosity [21]. But, for a first approach, the damping coefficient of the quartz resonator is

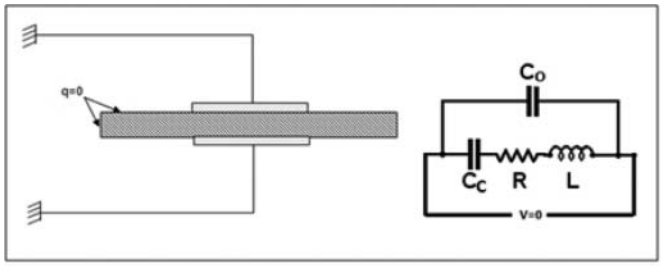

(a) Null electric charge

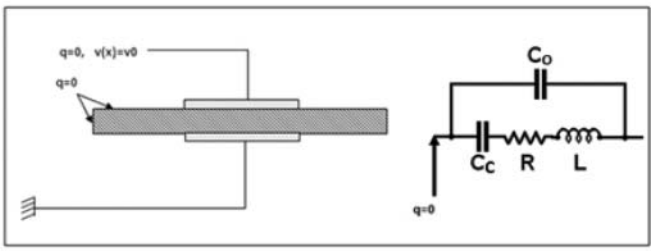

(b) Null electric potential

Fig. 7. Boundary conditions.

neglected.

$$f_r = \frac{1}{2\pi\sqrt{LC_c}}. \tag{26}$$

The second computation is performed for the parallel electrical circuit presented in Figure 7b. Relationships (27) can be written as:

$$\begin{aligned} u_0 &= u_c + u_L, \\ q_0 + q_c &= 0, \end{aligned} \tag{27}$$

where u_0, q_0, and q_c are the voltage in the static capacitance (V), the electric charge (C) across the static, and dynamic capacitance.

The natural frequency is given by Eq. (28):

$$f_a = \frac{\sqrt{1 + \frac{C_0}{C_c}}}{2\pi\sqrt{LC_c}}. \tag{28}$$

By combining Eqs. (28) and (26), motional parameters relationships (29) and (30) are obtained:

$$C_c = \left[\left(\frac{f_a}{f_r}\right)^2 - 1\right] C_0, \tag{29}$$

$$L = \frac{1}{4\pi^2 f_r^2 C_c}. \tag{30}$$

4. Mesh Optimization

In this section, the model mesh sensitivity is studied and a simple model in which the electrode mass effect is neglected is considered.

Let's note that the modeling approach with Comsol is quite different with respect to the other finite element analysis softwares. The studied physics are not included in specific finite elements. Comsol directly uses the Partial Differential Equations (PDEs). Indeed, the PDEs are directly discretized. The geometry is only a support for the PDEs and, for example, is used to define the boundary conditions.

4.1. *Computation Process*

The process initialization is based on the computation of an infinite plate equivalent to the studied resonator. In the case of an infinite plate, the natural frequencies are given by Eq. (31) [22]:

$$f_n = \frac{n}{2h} V_{66} = \frac{n}{2h}\sqrt{\frac{C_{66}}{\rho}}, \tag{31}$$

where n is the number of the studied overtone, h the thickness of the structure (m), V_{66} the sound velocity through the thickness axis, C_{66} the 66 elasticity coefficient (N.m^{-2}), and ρ the mass density of the quartz structure.

With Comsol Multiphysics, the natural frequencies and the antiresonance frequencies are computed around the three first overtones. The mechanical boundary conditions are a fixed side surface of the quartz plate ($\mathbf{u}_0 = 0$ in $\partial\Omega_0^u$) and the other surfaces free ($\bar{\mathbf{t}} = \mathbf{0}$ in $\partial\Omega_0^T$). The boundary conditions are presented in Figure 8. For the natural frequencies, electrodes are short-circuited ($v = v_a$ in $\partial\Omega_0^v$). For the antiresonance frequencies, the electrodes are open-circuited ($q_v = 0$ in $\partial\Omega_0^q$).

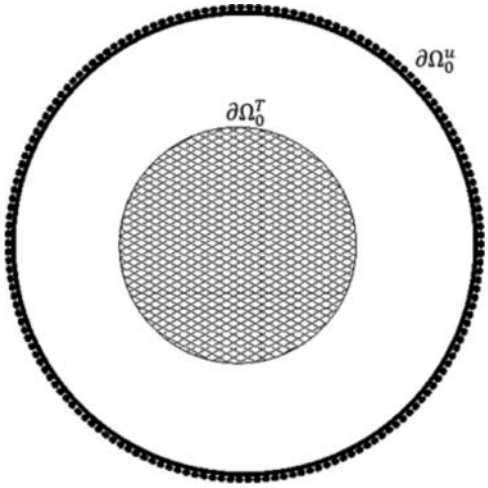

Fig. 8. Boundary conditions.

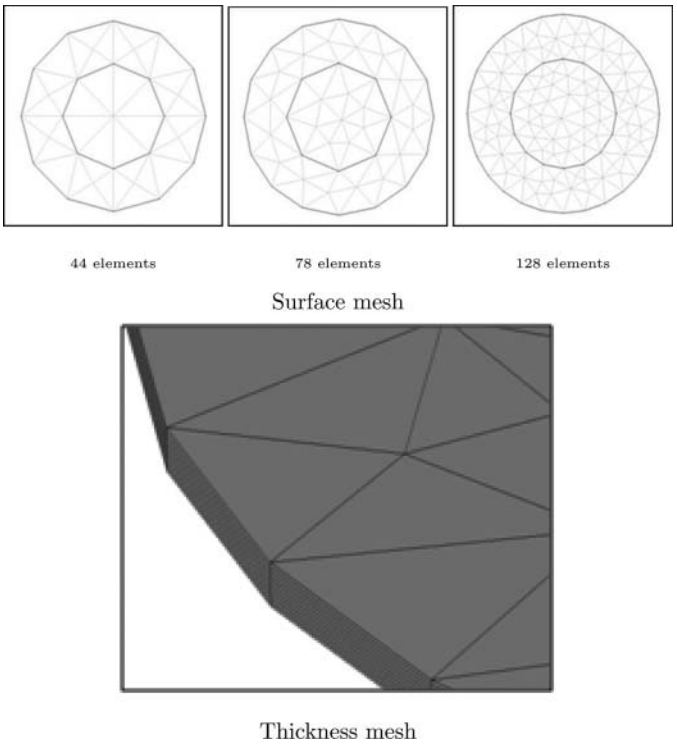

Fig. 9. Finite element discretization.

4.2. *Finite Element Discretization Cases*

The finite element discretization process is divided into two steps. First, the 2D surface of the quartz structure is meshed with Argyris finite elements [23]. Second, the surface mesh is extruded by layer to obtain the volumic mesh. So, the structure is meshed by Lagrange quadratic prismatic elements with six Gauss points. The advantage of this meshing process is the precise control of the finite element number in the thickness axis of the structure.

Three different surface meshes are analyzed. The first one contains 128 elements per layer, the second 78 elements, and the last 44 elements. For each mesh, the number of nodes in the thickness axis is studied. Figure 9 presents the specified meshes.

All computations are achieved with a laptop with the characteristics presented in Table 1.

4.3. *Numerical Results*

Let's note that, as presented in Figures 10 and 11, the number of nodes along the thickness axis strongly influence the fundamental frequency value. This value tends towards

Table 1. Computer characteristics

CPU	Intel Core 2 Duo Processor T5500 Frequency 1.66 Hz
Memory	1GB (533 Hz)

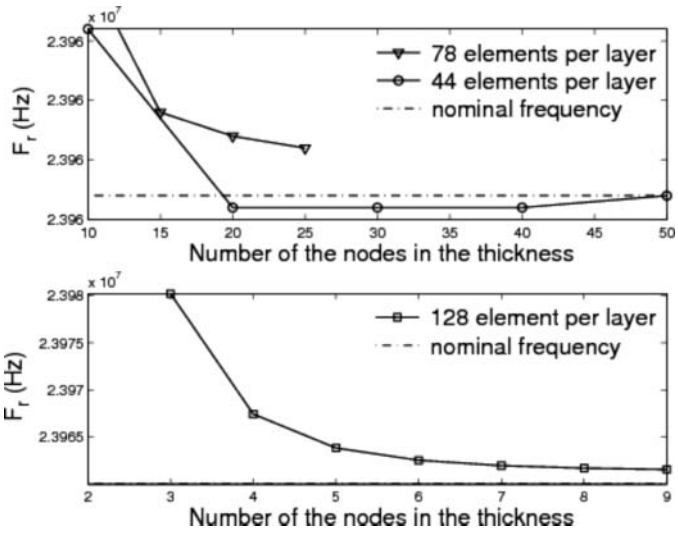

Fig. 10. Fundamental frequency with a null electric potential.

23.96007MHz and the antiresonance frequency tends towards 23.98173MHz. This value is obtained with ten nodes along the thickness axis and with the first surface mesh (128 elements per layer). As shown in Figures 12 and 13, the computation time considerably increases with the number of nodes along the thickness axis, in particular for the zero load case. Beyond nine nodes, which corresponds to 37,380 degrees of freedom, the computation becomes impossible because of out of memory. The additional stiffness in the antiresonance problem makes more complex and longer computations.

For the second surface mesh (78 elements per layer), the same value of frequency is obtained with 15 elements along the thickness axis. The number of nodes along the thickness axis is a more important parameter than the surface mesh for the resonance and antiresonance frequency accuracy. For the third surface mesh (44 elements per layer), the frequencies do not converge to the nominal values, as presented in Figure 10.

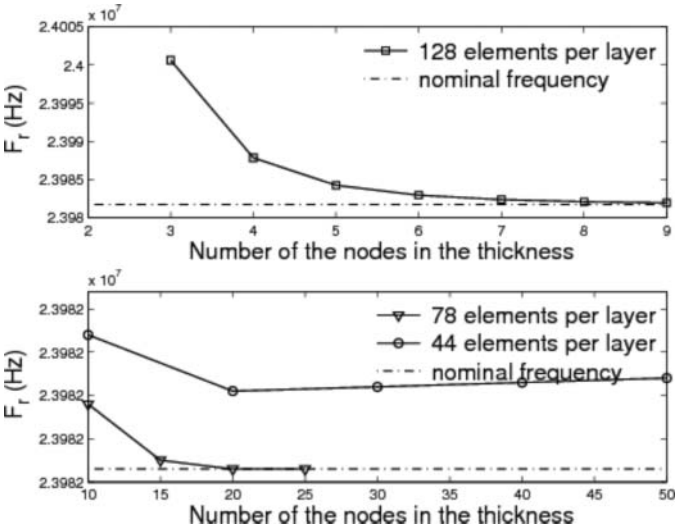

Fig. 11. Fundamental frequency with a null electric charge.

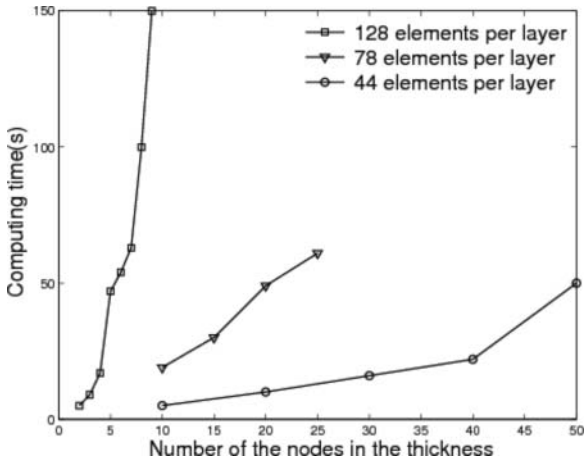

Fig. 12. Computation time for the fundamental frequency with a null electric potential.

So, the surface mesh is not the most important parameter for the computation accuracy but it is a necessary condition to converge the computation.

Basically, as presented in Figures 12 and 13, the computation time strongly increases with the number of surface degrees of freedom and thickness degrees of freedom. So, the second surface mesh with 20 nodes along the thickness axis makes it possible to have a good compromise precision/computation time. Indeed, by limiting at 20 nodes the number of nodes along the thickness axis, the relative error compared to the rated frequency does not exceed 0.5 ppm (part per million).

The same remarks on the evolution of the resonance and antiresonance frequencies can be underlined for the third and the fifth overtone, as presented in Figures 14–17. Let's note that, as shown in Figures 18–21, the computation times increase with the studied overtone number. The third surface mesh case is not analyzed for overtones due to the non-converged results for the fundamental frequencies.

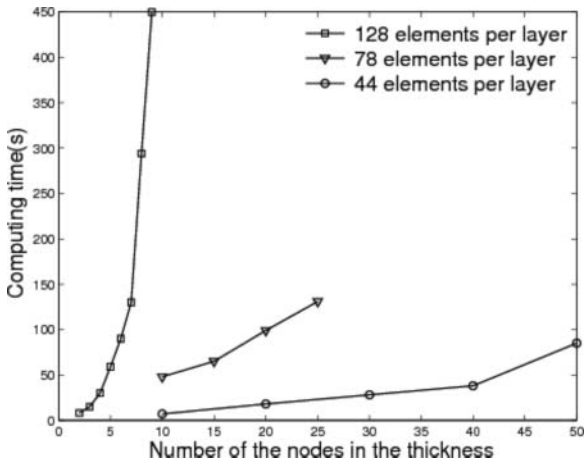

Fig. 13. Computation time for the fundamental frequency with a null electric charge.

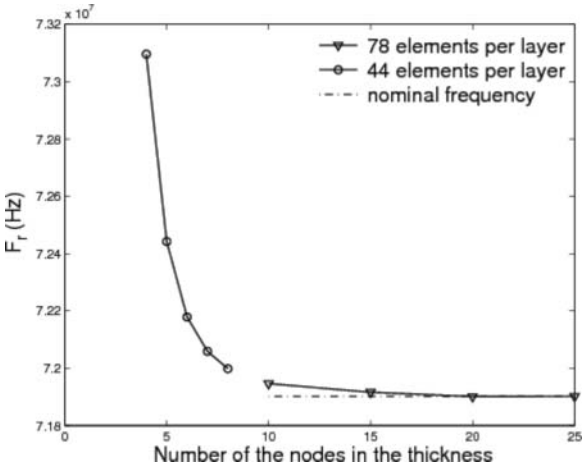

Fig. 14. Frequency for the third overtone with a null electric potential.

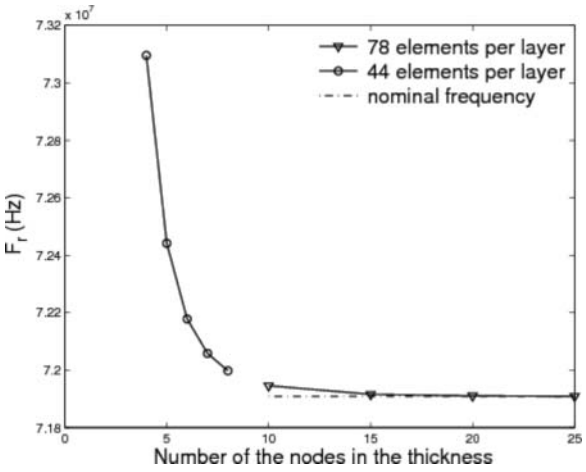

Fig. 15. Frequency for the third overtone with a null electric charge.

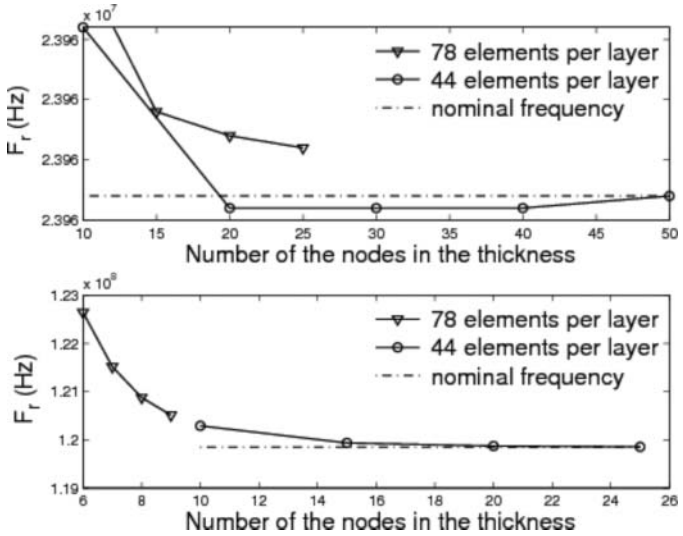

Fig. 16. Frequency for the fifth overtone with a null electric potential.

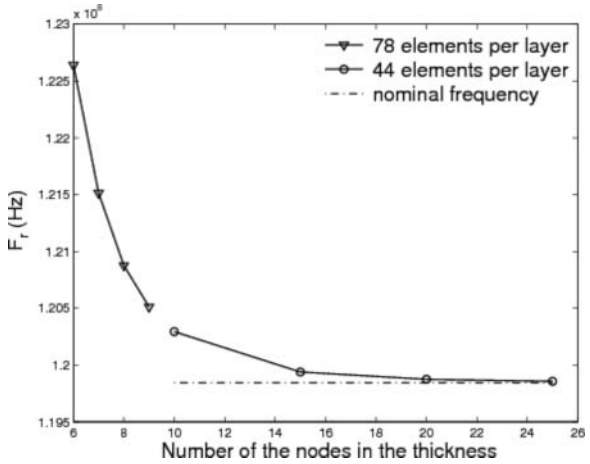

Fig. 17. Frequency for the fifth overtone with a null electric charge.

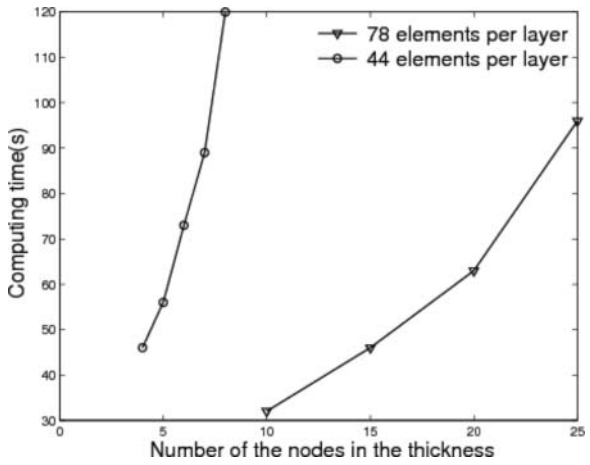

Fig. 18. Computation time for the third with a null electric potential.

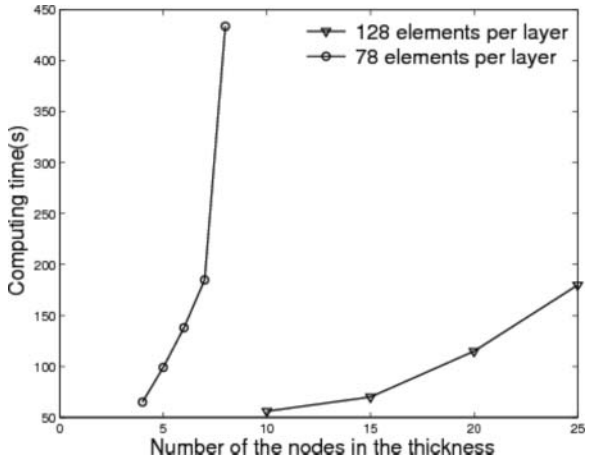

Fig. 19. Computation time for the third overtone with a null electric charge.

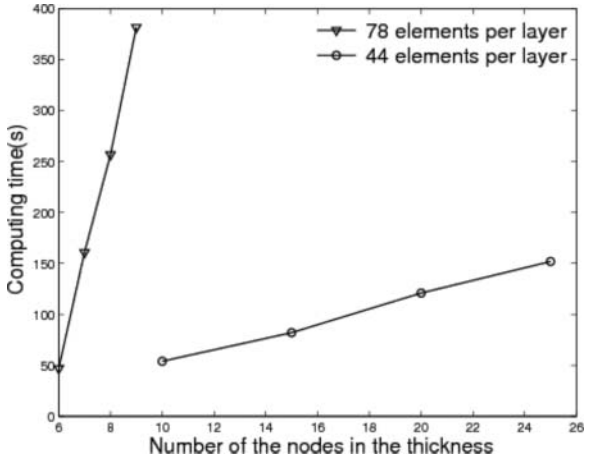

Fig. 20. Computation time for the fifth overtone with a null electric potential.

With the limitation at 20 nodes along the thickness axis, for the third overtone and in the second surface mesh case, the nominal resonance frequency is 71.90903 MHz. The relative error is approximately 111 ppm. The resonance frequency of the fifth overtone is 119.8456 MHz with a relative error of 204 ppm.

Thanks to a computation time/accuracy compromise, an optimal mesh can be chosen. The structure surface is discretized with 78 elements and, along the thickness axis, 20 nodes are selected. For the discretization along the thickness axis, a general criterion based on the sound wavelength ($\lambda_n = \frac{V_{66}}{f_n}$) can be applied. By combining Eq. (31), the wavelength formulation and the limitation of 20 nodes for the fifth overtone, the finite element size is determined by relationship (32):

$$Size_{finite\text{-}element} < \frac{\lambda_5}{20} = \frac{h}{50}. \tag{32}$$

This mesh will be used for all the simulations. In Table 2, the optimal results for the chosen mesh is given.

4.4. *Influence of Mesh Quality on Motional Parameters*

For simplicity, the surface mesh is fixed at 78 elements. Thus, the influence of the number of nodes along the thickness-axis

Table 2. Resonance frequencies and relative error with respect to converged value for the three overtones studied and for the optimal mesh (78 elements in surface and 20 elements along thickness-axis).

	Fundamental	Third overtone	Fifth overtone
Resonance frequencies (MHz)	23.96007	71.90903	119.8456
Relative error (ppm)	0.5	111	204

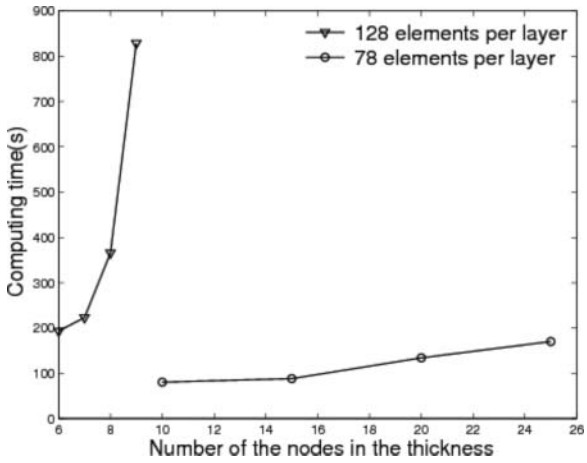

Fig. 21. Computation time for the fifth overtone with a null electric charge.

on the motional parameters is analyzed for the fundamental mode, the third overtone, and the fifth overtone.

As presented in Figure 22, the number of nodes along the thickness-axis implies a motional inductance maximal relative variation of 1% for the fifth overtone, 0.12% for the third overtone, and less than 0.001% for the fundamental mode.

Figure 23 shows the motional capacitance evolution with respect to the number of nodes along the thickness-axis for the fundamental mode, the third overtone, and the fifth overtone. The motional capacitance value is very sensitive to the number accuracy of the resonance and antiresonance frequencies. The value variations are 2% for the fifth overtone, 0.4% for the third overtone, and less than 0.001% for the fundamental mode.

With the chosen mesh setup, the motional parameters are presented in Table 3.

Table 3. Optimal motional parameters for the chosen finite element discretization

	$L_s(mH)$	$C_s(fF)$
Fundamental mode	4.94	8.94
Third overtone	3.84	1.28
Fifth overtone	2.96	0.596

5. Mass-Loading Effects

The electrode mass has an effect on resonator frequency value [24]. In this part, three different models are introduced and compared so as to analyze the mass-loading effects.

5.1. *Mass-Loading Models*

The first model is the reference model. The electrodes mass are neglected. This model is called simple model. The second model consists in homogenizing the mass densities in the contact area between the electrodes and the quartz structure. The equivalent density ρ_h is given by Eq. (33). This model is called the homogenized model.

$$\rho_h = \frac{2\rho_e h_e + \rho_q h_q}{2h_e + h_q}, \tag{33}$$

where (ρ_e, h_e) and (ρ_q, h_q) are respectively the mass densities ($kg.m^{-3}$) and the stiffnesses ($N.m^{-2}$) of the electrodes and the quartz structure.

In the third model, the electrodes are modeled by a finite element method. For each electrode, 78 surface elements are considered for one thickness element. This model is called the complete model. Figure 24 illustrates these three models.

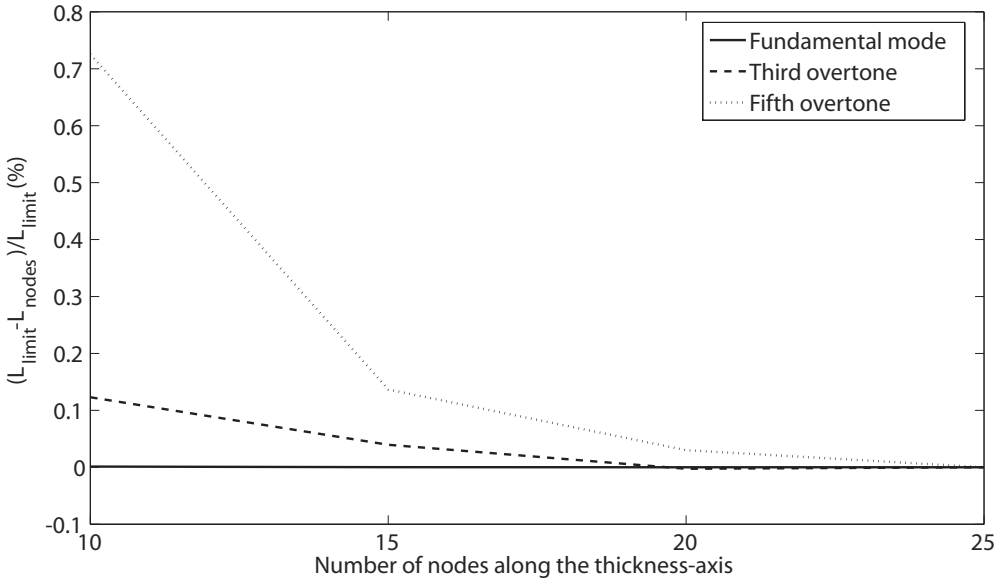

Fig. 22. Motional inductance with respect to number of nodes along the thickness-axis for the fundamental mode, the third overtone, and the fifth overtone.

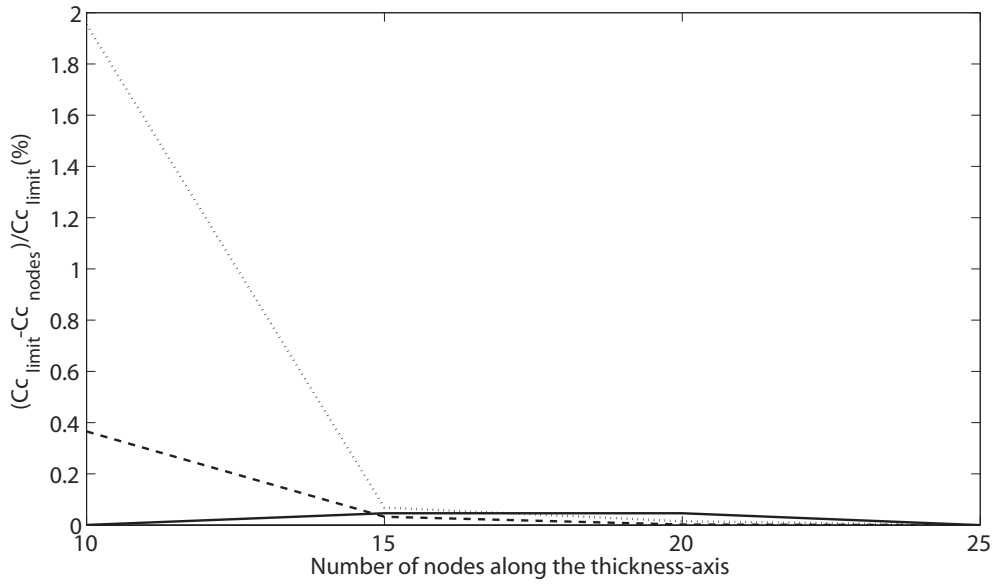

Fig. 23. Motional capacitance with respect to number of nodes along the thickness-axis for the fundamental mode, the third overtone, and the fifth overtone.

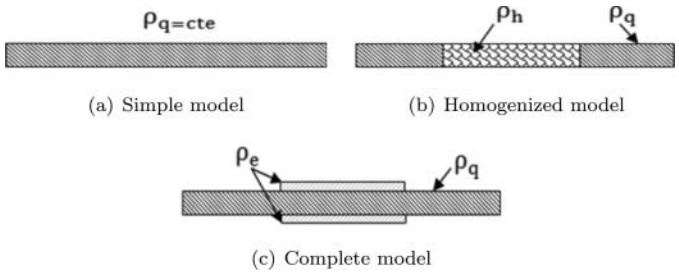

Fig. 24. Resonator models.

The resonator actuating electrodes can be made in different materials: aluminum (Al), silver (Ag), gold (Au), and platinum (Pt).

5.2. *Numerical Results*

In this subsection, the influence of the type of electrode modeling and the four different electrode materials on the thickness-shear modes is analyzed. The computation process developed for the mesh sensitivity study is kept. Tables 4 to 9 summarize the numerical results dealing with the natural and

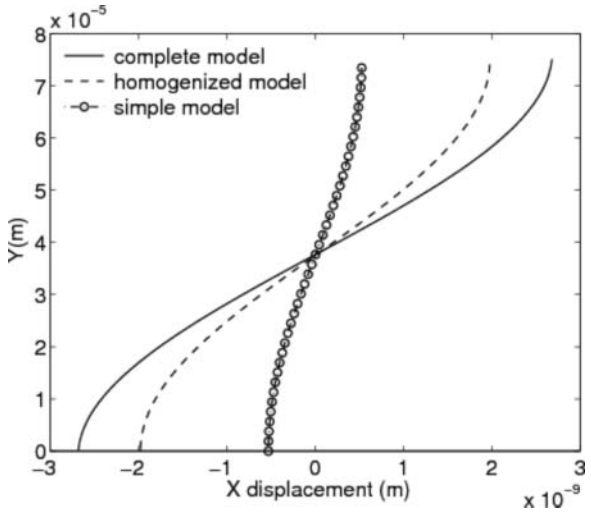

Fig. 25. Modal deformation with respect to the modeling type for the fundamental mode (X displacement).

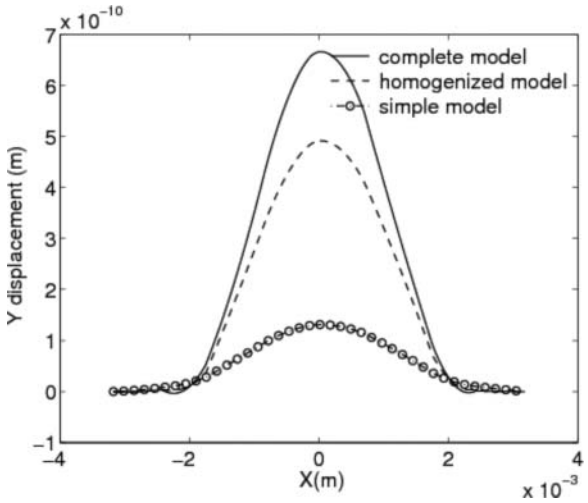

Fig. 26. Modal deformation with respect to the modeling type for the fundamental mode (Y displacement).

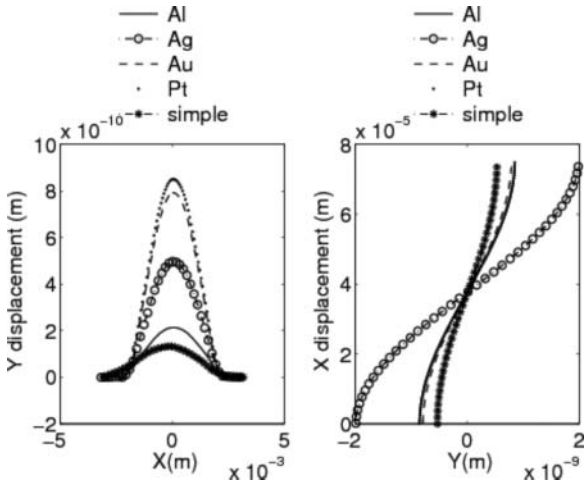

Fig. 27. Modal deformations with respect to the electrode material for the fundamental mode.

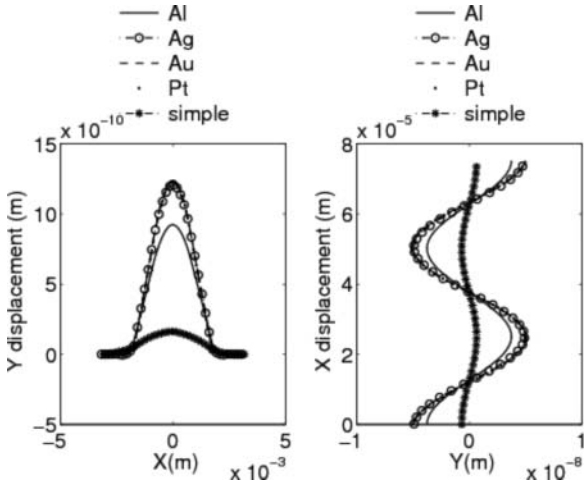

Fig. 28. Modal deformations with respect to the electrode material for the third overtone.

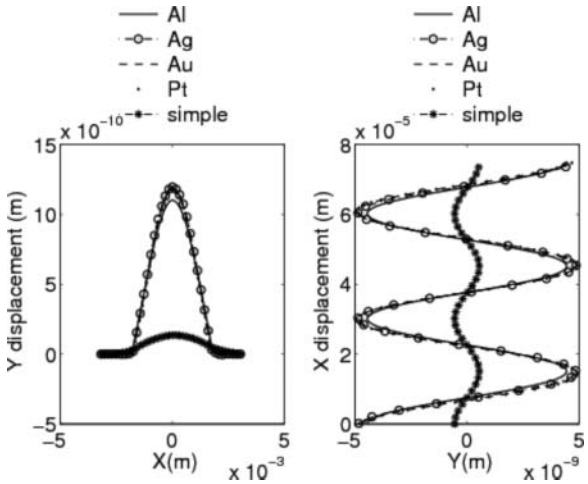

Fig. 29. Modal deformations with respect to the electrode material for the fifth overtone.

Table 4. Frequencies [MHz] for aluminium electrodes

	Fundamental		Third overtone		Fifth overtone	
Model	Fr	Fa	Fr	Fa	Fr	Fa
Simple	23,960	23,981	71,901	71,910	119,840	119,847
Homogenized	23,959	23,980	71,901	71,907	119,865	119,869
Complete	23,867	23,886	71,613	71,618	119,384	119,387

Table 5. Frequencies [MHz] for silver electrodes

	Fundamental		Third overtone		Fifth overtone	
Model	Fr	Fa	Fr	Fa	Fr	Fa
Simple	23,960	23,981	71,901	71,910	119,840	119,847
Homogenized	23,825	23,843	71,484	71,490	119,170	119,173
Complete	23,593	23,611	70,783	70,788	118,004	118,006

Table 6. Frequencies [MHz] for gold electrodes

	Fundamental		Third overtone		Fifth overtone	
Model	Fr	Fa	Fr	Fa	Fr	Fa
Simple	23,960	23,981	71,901	71,910	119,840	119,847
Homogenized	23,672	23,690	71,021	71,027	118,398	118,401
Complete	23,290	23,307	69,879	69,884	116,518	116,521

Table 7. Frequencies [MHz] for platinum electrodes

	Fundamental		Third overtone		Fifth overtone	
Model	Fr	Fa	Fr	Fa	Fr	Fa
Simple	23,96	23,981	71,901	71,910	119,840	119,847
Homogenized	23,63	23,653	70,910	70,915	118,212	118,215
Complete	23,22	23,236	69,669	69,674	116,182	116,185

Table 8. Acceleration sensitivity

Material	$\Gamma_a(10^{-12}/g)$
Simple	2,48
Aluminum	3,19
Silver	13,24
Gold	14,03
Platen	14,18

Table 9. Frequency and motional parameters (fifth overtone) for a resonator with standard quartz SC and silver electrodes

	Measurements	Modeling	Relative difference (%)
Frequency (MHz)	120.0015	118.004	1.65
Static capacitance (pF)	4.7	5.1	8.53
Dynamic capacitance (fF)	0.183	0.173	5.46
Inductance (mH)	9.7	10.53	8.56
Resistance (Ω)	75.2	0	—

antiresonance frequencies for the first three overtones and for the different electrode materials.

Basically, the results show that the simple model gives an approximation rather representative of the aluminum electrodes. Indeed, the mass density of this last material (2700 kg/m^3) is close to the quartz mass density (2648.1 kg/m^3). In this case, the relative error of the frequencies compared to the complete model is less than 0.4%. For other materials, the error is more important, it amounts to 0.6% for silver (10500 kg/m^3), 2.9% for gold (19300 kg/m^3) and 3.2% for platinum (23000 kg/m^3).

The electrode mass density has a strong influence on the modal shapes. The vertical and thickness-shear displacements in the center of the plate increase when the electrode mass density increases. With respect to overtones, this influence is more important, as shown in Figures 25–29.

The validity of the simplified model depends on the difference between the quartz mass density and the electrode mass density. Indeed, the more the electrode mass density is high the more the mass-loading effects are important. Let's also note that the homogenized model makes it possible to improve the approximation without modifying the computation time. It allows to take into account the electrode mass effects. This model will be used to study the acceleration effects in the next section.

5.3. *Influence of Mass-Loading Effects on Motional Parameters*

For clarity of figures, the data, presented in Figures 30 and 31, are normalized. For Figure 30, the chosen normalization is $\frac{L_{\text{simple for overtone considered}} - L_{\text{model considered}}}{L_{\text{simple for overtone considered}}}$. For figure 31, the chosen normalization is $\frac{C_{\text{model considered}}}{C_{\text{simple for overtone considered}}}$ because the dispersion between the different values is very strong.

The error on the electrical values is strongly related to the type of modeling. Basically, the error with respect to the simple model electric inductance increases with the electrode mass. In absolute, the simple model overestimates the electric inductance value. The electromechanical equivalence explains this tendency. Let's note that error is not sensitive to the overtone considered.

For the equivalent electric capacitance, the error with respect to the simple model becomes very important with the high overtones. The electric capacitance values are very low and so very sensitive to the computations. There is no clear tendency with respect to the electrode material or the type of modeling even if a modeling improvement can be assumed with the taking into account of the electrode mass.

6. Acceleration Sensitivity

In this section, the acceleration sensitivity of the resonator is studied. The influence of the various materials and acceleration on the natural frequencies is focused on.

6.1. *Computation Process*

The taking into account of the acceleration sensitivity requires a computation in large deformations. In this case, the tensor of deformation is given by Eq. (34):

$$\mathbf{S} = \frac{1}{2}(\nabla \mathbf{u} + \nabla \mathbf{u}^t) + \frac{1}{2}\nabla \mathbf{u}^t \mathbf{u}. \tag{34}$$

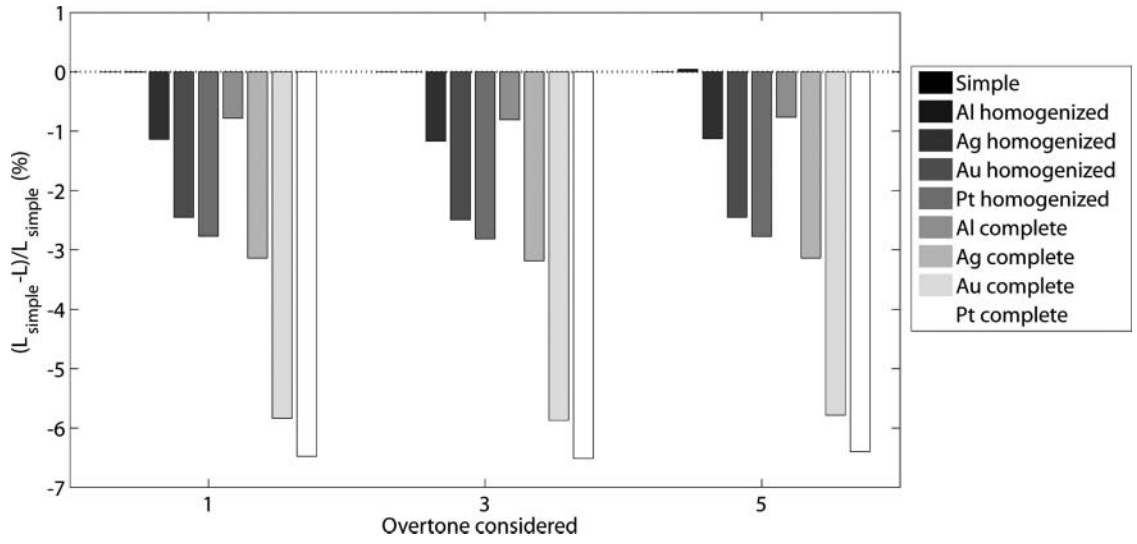

Fig. 30. Evolution of motional inductance with respect to electrode material and type of modeling.

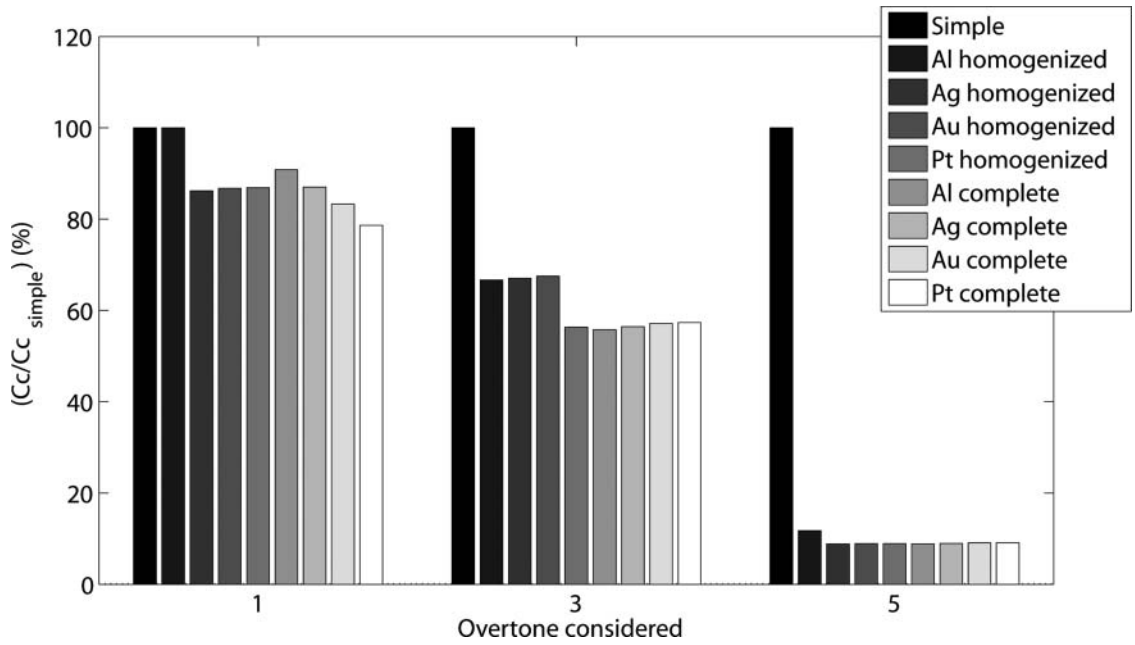

Fig. 31. Evolution of motional capacitance with respect to electrode material and type of modeling.

The computation is made in two steps. First, a static problem where the load is an acceleration equivalent volumic force is solved. Figure 32 depicts the deformed structure for this type of load. In the second step, the eigenvalue problem is solved by considering the static result as initial conditions.

The acceleration sensitivity is defined by Eq. (35) [11]:

$$\Gamma_a = \frac{f_{acc} - f}{Af}, \tag{35}$$

where f_{acc}, f are respectively the frequency (Hz) considering the acceleration field and frequency without acceleration, and A is the acceleration module ($\mathrm{m.s^{-2}}$).

6.2. *Numerical Results*

Figures 33 to 35 show the relative variation of the fundamental frequencies with respect to the acceleration (expressed in $g = 9.81\mathrm{m.s^{-2}}$), applied in the three axes, and for each type of electrode material. Along the thickness axis, let's note that the acceleration sensitivity increases in a parabolic way according to the acceleration magnitude. For low acceleration values (lower than 30 g), a linear variation can be assumed. Hence, the directing coefficient represents the acceleration sensitivity. Table 8 summarizes their values for each material. These values are in good agreement with Tiersten's results [25]. Let's note that the acceleration sensitivity increases with the electrode mass density. This fact led to the development of a new resonator class: the BVA resonator. It was introduced by Besson [26]. One of the major distinguishing characteristics of the BVA resonator is that the electrodes are not deposited on the resonator active vibrating area so as to limit the acceleration sensitivity.

Along the thickness axis, the acceleration has a hardening effect on the structure. Therefore, the frequencies increase according to the acceleration as presented in Figure 34. For the axis X and Z, a softening effect is observed for the setup considered as shown in Figures 33 and 35. However, in the structure plan, the effect depends strongly on the load direction with respect to the crystallographic axes, as depicted in Figure 36.

6.3. *Influence of Acceleration Sensitivity on Motional Parameters*

The difference between the resonance and antiresonance frequencies is due to the piezoelectric coupling coefficient and the electrode location. The acceleration field does not induce modifications of these two parameters at first order. Thus,

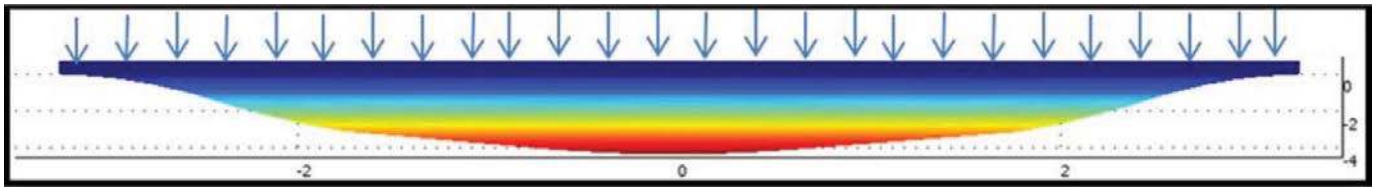

Fig. 32. Static load (color figure available online).

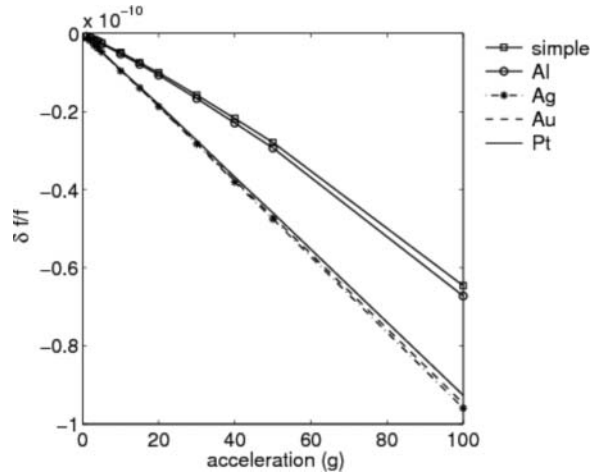

Fig. 33. Evolution of fundamental frequency variation with respect to acceleration magnitude according X axis.

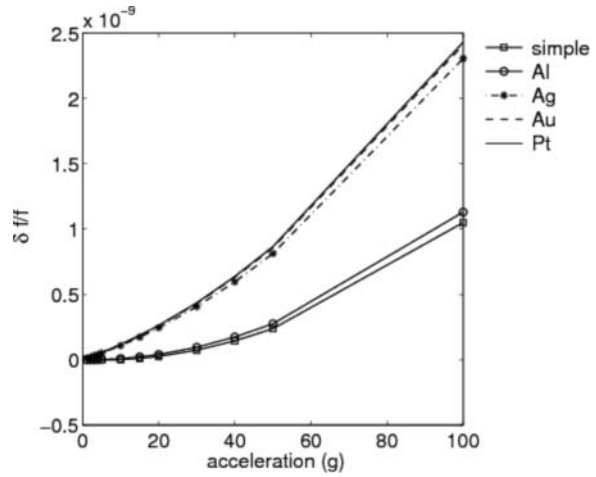

Fig. 34. Evolution of fundamental frequency variation with respect to acceleration magnitude according to Y axis.

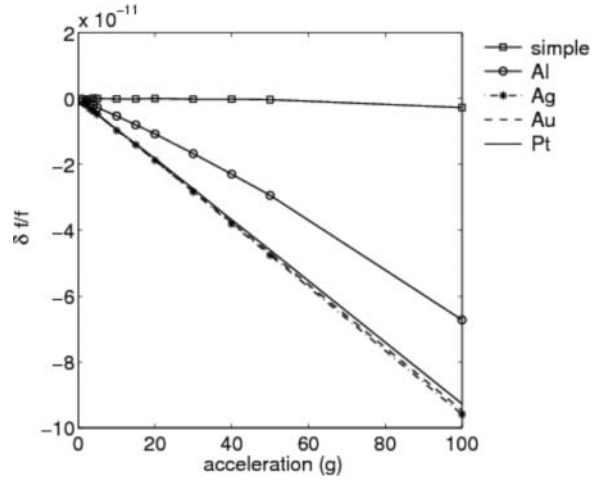

Fig. 35. Evolution of fundamental frequency variation with respect to acceleration magnitude according to Z axis.

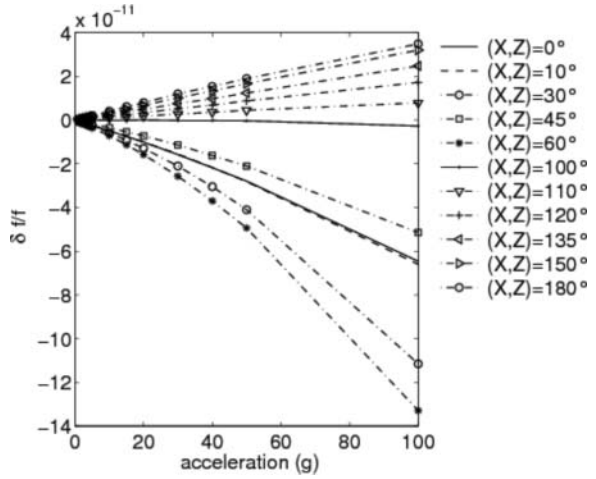

Fig. 36. Fundamental frequency variation with respect to the angle between the acceleration direction and the Z axis for the simple model.

the influence of the acceleration field on the resonance and antiresonance frequencies can be considered homothetic.

Consequently, thanks to Eq. (35), Eqs. (36) and (37) can be written as:

$$f_r acc = (A\Gamma_a + 1) fr, \tag{36}$$

$$f_a acc = (A\Gamma_a + 1) fa. \tag{37}$$

Then, the influence of the acceleration field on the motional parameters can be developed through Eqs. (38) and (39). Let's note that only motional inductance is modified by the acceleration endured by the resonator. The electromechanical equivalence, presented in Figure 6, shows that the motional inductance represents the vibrating mass of the crystal unit. Basically, this vibrating mass is forced by the acceleration field.

$$C_c acc = \left[\left(\frac{f_a acc}{f_r acc} \right)^2 - 1 \right] C_0 = C_c, \tag{38}$$

$$Lacc = \frac{1}{4\pi^2 f_r acc^2 C_0} = \frac{L}{(A\Gamma_a + 1)^2}. \tag{39}$$

Figure 37 depicts the motional inductance evolution with respect to the acceleration magnitude along the Y axis, the most forced resonator axis. Let's remark that the electrode material has a large influence of the motional inductance values. But, in absolute, the motional parameter modification due to the acceleration field is relatively limited, less than 1 ppb (part per billion).

7. Experimental Data

In order to check the validity of the numerical model, a comparison between numerical data and experimental date is provided. One hundred standard quartz SC-resonators with silver

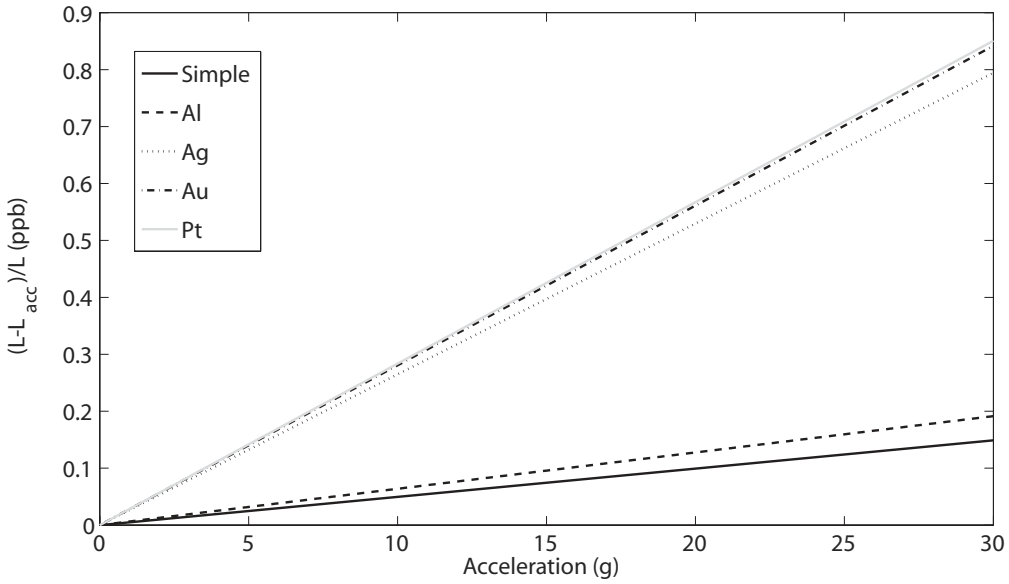

Fig. 37. Evolution of motional inductance with respect to acceleration magnitude according Y axis.

electrodes made by Temex, are measured. Table 9 illustrates the differences between the results of the numerical model and experimental measurements. Let's note that the results of the numerical model are close to experimental data. The variations remain important in particular for the motional parameters. These variations can be related to several parameters. First, the mechanical boundary conditions considered in the model are different with respect to the ones of the devices. Indeed, in the numerical model, the side edges of the quartz resonator are embedded, whereas the real resonator device has four fixing points. Consequently, the static stress endured by the active structure is quite different and can explain the frequency value difference and the modification of the gap between the natural resonance frequency and the natural anti-resonance frequency. Moreover, in the numerical modeling, the damping factor is neglected and the quartz material parameters used in the modeling is extracted from the literature and not issued from measurements. Consequently, the relative difference between the different analyzed values is quite limited with respect to the complexity of the structure and the computation assumptions.

8. Concluding Remarks

In this article, the influence of the model mesh quality, the electrode mass-loading, and the acceleration field on the motional parameters of a quartz resonator are investigated. A SC-cut quartz resonator is analyzed for its fundamental thickness-shear resonance, the third and the fifth overtone. A simple computation method in order to answer at the industrial time constraints is developed. A Butterworth-Van Dyke (BVD) model based on an electrical equivalent circuit with, as input data, the studied natural frequency and the antiresonance frequency of an accurate finite element modeling is used. The finite element model has been implemented in a commercial software called Comsol.

The different modeling steps and its limitations are shown. So as to have a good approximation of the motional parameters, it is essential to have a precise finite element discretization along the thickness axis. The number of nodes become more and more critical with the overtone number. In a second step, for more accuracy, the electrode mass-loading is taken into account. The electrode material strongly influences the motional parameters and the modal shape amplitudes. In a third step, the acceleration influence on the motional parameters is studied. The acceleration sensitivities obtained for the different electrode materials are in good agreement with the literature. The acceleration field has a very limited influence on the motional parameters. Consequently, it is not necessary to take it into account at first order. Finally, the experimental data confirm the validity of the numerical model.

References

[1] J.P. Valentin, G. Thiobald, and J.J. Gagnepain, Frequency shifts arising in-plan temperature gradient distribution in quartz resonators, Proceedings of the 38th Annual Symposium on Frequency Control, pp. 157–163, 1984.

[2] D. Janiaud, R. Besson, J.J. Gagnepain, and M. Valdois, Quartz resonator thermal transient due crystal support, Proceedings of the 35th Annual Symposium on Frequency Control, pp. 340–344, Fort Monmouth, NJ, 1981.

[3] Y.-K. Yong, M. Patel, J. Vig, and A. Ballato, Effects of electromagnetic radiation on the Q of quartz resonators, IEEE Trans. Ultrason., Ferroelec., Freq. Contr., vol. 56, no. 2, pp. 353–360, 2009.

[4] C.R. Dauwalter, The temperature dependence of the force sensitivity of AT-cut quartz crystals, Proceedings of the 26th Annual Symposium on Frequency Control, pp. 108–112, 1972.

[5] E.P. EerNisse, Calculations on the stress compensated (SC-Cut) quartz resonator, Proceedings of the 30th Annual Symposium on Frequency Control, pp. 8–11, 1976.

[6] A. Ballato, Doubly rotated thickness mode plate virators, Phys. Acous., vol. 13, pp. 115–181, 1977.

[7] J.R. Vig and T.R. Mecker, The aging of bulk acoustic wave resonators, filters and oscillators, Proceedings of the 45th Annual Symposium on Frequency Control, pp. 77–101, 1991.
[8] A.W. Warner, Design and performance of ultraprecise 2.5-mc quartz crystals units, Bell Sys. Tech. J., vol. 34, pp. 1193–1217, 1960.
[9] R.B. Haskell, P.E. Morley, and D.S. Stevens, High Q precision SC cut resonators with low acceleration sensitivity, Proceedings of the 56th Annual Symposium on Frequency Control, pp. 111–118, 2002.
[10] R.B. Haskell, J.E. Buchanan, P.E. Morley, B.B. Desai, M.A. Esmiol, M.E. Martin, and D.S. Stevens, State-of-the-art in the design and manufacture of low acceleration sensitivity resonators, Proceedings of the Frequency Control Symposium and Exposition IEEE, pp. 672–677, 2004.
[11] M.S. Patel and Y.-K. Yong, Application of a DC Bias to reduce acceleration sensitivity in quartz resonators, Proceedings of the Ultrasonics Symposium IEEE, pp. 270–273, 2004.
[12] Y. Meyer and M. Collet, Active damping of "parasitic" vibration modes of a quartz sensor, Smart Mater. Struct., vol. 17, no. 6, 065006, 2008.
[13] Y.-K. Yong, M.S. Patel, S. Srivastava, M. Tanaka, and T. Imai, The impact of finite element analysis on the design of quartz resonators, Proceedings of the International Frequency Control Symposium and Exposition, IEEE, pp. 9–22, 2006.
[14] P. C.Y. Lee, N. Liu, and A. Ballato, Thickness vibrations of a piezoelectric plate with dissipation, *IEEE Trans. Ultrason.*, *Ferroelec.*, *Freq. Contr.*, vol. 51, no. 1, pp. 52–62, 2004.
[15] Y.-K. Yong, M.S. Patel, and M. Tanaka, Effects of thermal stresses on the frequency-temperature behavior of piezoelectric resonators, J. Therm. Stresses, vol. 30, no. 6, pp. 639–661, 2007.
[16] R. Simkovics, H. Landes, M. Kaltenbacher, and R. Lerch, Nonlinear finite element analysis of piezoelectric transducers, Proceedings of the Ultrasonics Symposium IEEE, pp. 1057–1060, 1999.
[17] S.Y. Pao, M.K. Chao, T. Wang, D. Chang, C.S. Lam, and P.Z. Chang, Parameters extraction and design optimization for AT-cut quartz resonator based on Mindlin's 2D model, Proceedings of the International Frequency Control Symposium and Exposition, IEEE, pp. 36–39, 2006.
[18] R. Bechman, Elastic and piezoelectric constants of Alpha-Quartz, Phys. Rev., vol. 110, no. 5, pp. 1060–1061, 1958.
[19] B.A. Auld, Acoustic Fields and Waves in Solids, (Vol. 1-2, 2nd Edition, Krieger Publishing Company, Malabar, FL, 1990.
[20] M. Naillon, R.H. Coursant, and F. Besnier, Analyse de structures pizolectriques par une mthode d'éléments finis (text in French), Acta Elec., vol. 25, no. 4, pp. 341–362, 1983.
[21] J. Wang, W. Zhao, J. Du, and Y. Hu, The calculation of electrical parameters of AT-cut quartz crystal resonators with the consideration of material viscosity, Ultrasonics, vol. 51, no. 1, pp. 65–70, 2010.
[22] H.F. Tiersten, Linear Piezoelectric Plate Vibration, Plenum Press, New York, 1969.
[23] J. Argyris, L. Tenek, and L. Olofsson, TRIC: A simple but sophisticated 3-node triangular element based on 6 rigid-body and 12 straining modes for fast computational simulations of arbitrary isotropic and laminated composite shells, Comput. Methods Appl. Mech. Eng., vol. 145, p. 1185, 1997.
[24] J.R. Vig and A. Ballato, Frequency control devices, In: Ultrasonic Instruments and Devices, U.S. Army Communications Electronics Command, Fort Monmouth, NJ, 1999.
[25] H.F. Tiersten, Analytical Investigation of the Acceleration Sensitivity of Acoustic Bulk and Surface Wave Resonators, Rensselaer Polytechnic Inst. Troy, NY, 1991.
[26] R.J. Besson, A new electrodeless resonator design, Proceedings of the 31st Annual Symposium on Frequency Control, pp. 147–152, Fort Monmouth, NJ, 1977.